Li-Ion Batteries Hot Paper

How to cite: *Angew. Chem. Int. Ed.* **2022**, *61*, e202202731
International Edition: doi.org/10.1002/anie.202202731
German Edition: doi.org/10.1002/ange.202202731

Formation of LiF-rich Cathode-Electrolyte Interphase by Electrolyte Reduction

Panxing Bai, Xiao Ji, Jiaxun Zhang, Weiran Zhang, Singyuk Hou, Hai Su, Mengjie Li, Tao Deng, Longsheng Cao, Sufu Liu, Xinzi He, Yunhua Xu, and Chunsheng Wang**

Abstract: The capacity of transition metal oxide cathode for Li-ion batteries can be further enhanced by increasing the charging potential. However, these high voltage cathodes suffer from fast capacity decay because the large volume change of cathode breaks the active materials and cathode-electrolyte interphase (CEI), resulting in electrolyte penetration into broken active materials and continuous side reactions between cathode and electrolytes. Herein, a robust LiF-rich CEI was formed by potentiostatic reduction of fluorinated electrolyte at a low potential of 1.7 V. By taking $LiCoO_2$ as a model cathode, we demonstrate that the LiF-rich CEI maintains the structural integrity and suppresses electrolyte penetration at a high cut-off potential of 4.6 V. The $LiCoO_2$ with LiF-rich CEI exhibited a capacity of 198 mAh g^{-1} at 0.5C and an enhanced capacity retention of 63.5 % over 400 cycles as compared to the LiF-free $LiCoO_2$ with only 17.4 % of capacity retention.

Introduction

Portable electronic devices and automobiles demand high-energy-density Li-ion batteries.[1] One pragmatic and possible way is to elevate the upper cut-off voltage of the transition metal oxide cathodes from 4.3 V to 4.6/or 4.7 V, which can increase the discharge capacity and energy density by 15–35 %.[2–4] However, more Li insertion/extraction in these transition metal oxides also increases the volume change, resulting in cracking for both transition metal oxide and cathode-electrolyte interphase (CEI). Therefore, the electrolyte will penetrate into cracked transition metal oxide and react with it.[5–11] The continuous side reactions of transition metal oxide with electrolyte induce a fast capacity decay. Recent findings demonstrated that the volume change-induced cracks in transition metal oxide cathodes can be suppressed or reversibly recovered if the electrolyte is blocked by robust CEI layers,[4,12–16] which will significantly enhance the cathode cycle life even at a high cut-off voltage. The challenge is how to form a robust CEI that can accommodate the large volume change. Among the known CEI, the organic-rich CEI is bonded to the cathode surface and cannot withstand the large volume change of the cathode, resulting in breakage during lithiation/delithiation and continuous parasitic reactions between the cathode and the electrolytes. In addition, organic-rich CEI is easily oxidizable at a high voltage, which further accelerates capacity decay.[17–21] In contrast, the inorganic-rich CEI, especially LiF-rich CEI, has a weak bond to transition metal oxide cathodes, which will suffer less strain/stress during the volume change of the cathode, thus maintaining the protection. In addition, LiF-rich interphase is also very thin due to an extremely low electronic conductivity of LiF, and has a wide electrochemical stability window, endowing it with good passivation capability for both cathodes and anodes.[22–26]

However, the formation of LiF-rich CEI on transition metal oxides is also very challenging. In the commercial carbonate electrolytes, the CEI on the cathode was formed mainly by oxidation or catalytic decompositions of solvents and CEI is mainly composed of organic components.[21,27] The high degree of fluorine substitution in the carbonates/ethers/sulfones/cyclic phosphate solvents renders some stable polymers and LiF in CEI upon oxidation.[4,14,28–32] The concentration of LiF and inorganic fragments in CEI can be further enhanced in a highly concentrated/localized highly concentrated or ionic liquid electrolyte,[33–38] but it's still very challenging because direct defluorination via oxidation of these anions, such as FSI^- and PF_6^-, were found to be unavailable owing to the high reaction energies or occurring at higher potentials.[39–41] Although LiF can be produced from the hydrolysis of PF_6^-, it's accompanied with the generation of erosive HF, and thus CEI is not dense and resistive.[42] Some special salts with high HOMO (highest occupied molecular orbital), such as LiDFOB, can be oxidized preferentially ($\approx$4.2 V vs Li^+/Li) on the delithiated cathode before the bulk electrolyte solvents participate,

[*] P. Bai, X. Ji, J. Zhang, W. Zhang, S. Hou, T. Deng, L. Cao, S. Liu, X. He, C. Wang
Department of Chemical and Biomolecular Engineering, University of Maryland
College Park, MD 20742 (USA)
E-mail: cswang@umd.edu

P. Bai, H. Su, M. Li, Y. Xu
School of Materials Science and Engineering, Tianjin University
Tianjin 300072 (China)
E-mail: yunhua.xu@tju.edu.cn

whereas still forming polymeric B-containing component.[43–45] Recently, it was reported that the amount of LiF in CEI can be increased through the synergy between O_2^- and fluorinated ether (HFE) by introducing a Li_2O sacrificial agent and HFE additive.[46] However, O_2^- also attacks the other solvents.

In contrast, LiF-rich interphase can be easily formed by reduction of anions at a low potential below 1.0 V in carbonate or ether electrolytes.[17,25,40] To form LiF-rich CEI on cathode, an electrolyte with a higher reduction potential above the decomposition potential of transition metal oxide cathode is required.[47–49] The reduction potential of electrolyte can be elevated by choosing highly-reductive salts or raising ionic aggregation ratio through increasing salt concentration or using weak-solvated solvents.[23,34,39,50] For example, LiDFOB or concentrated LiFSI can be reduced at relatively high potential to form LiF and other inorganics.[50–53] If the reduction potential is also stable to the cathode, the robust LiF-rich interphase can stabilize both the cathode and anode at the same time. Although direct external electrical shorting between anode and cathode can form uniform interphase on cathodes, it may cause the decomposition of transition metal oxide cathodes.[54] To form LiF-rich CEI, cathode should be discharged to a potential that only fluorinated electrolyte is reduced but cathode is still stable.

In this work, a dense LiF-rich CEI was formed on a single-crystalline $LiCoO_2$ (LCO) cathode after potentiostatic reduction at 1.7 V in 1.0 M LiDFOB-0.2 M $LiBF_4$-FEC-DEC electrolyte, since the electrolyte reduction potential of 1.7 V is higher than the reduction potential of LCO cathode.[47,52,55–58] LiF-rich CEI restrains the structural damage of LCO, detrimental oxidative decomposition of solvents and dissolution of Co into electrolyte even at the high cut-off voltage of 4.6 V. The LCO with LiF-rich CEI achieved an excellent cyclability with a capacity of 198 mAh g^{-1} and retention of 63.5 % over 400 cycles at 0.5C (100 mA g^{-1}, 1C rate corresponds to a specific current of 200 mA g^{-1}) as compared to the LiF-free LCO with only 17.4 % of capacity retention. Also, the LCO//graphite full cell with LiF-rich CEI on LCO maintained 85 % of capacity after 500 cycles. The formation of LiF-rich CEI on cathode by pre-potentiostatic discharging is universal and can be applied on all high energy cathodes to achieve long cycle life.

Results and Discussion

1.0 M LiDFOB–0.2 M $LiBF_4$-FEC-DEC (denoted as LiDFOB-$LiBF_4$) was selected as a model electrolyte because the LiF can be formed by reduction of salts at a high reduction potential.[52,55,56] The reduction and oxidation potentials of LiDFOB-$LiBF_4$ electrolyte were measured using linear sweep voltammetry (LSV) in Li//stainless-steel (SS) half-cells. As indicated in Figure S1a, a reduction starts at 1.9 V with peak current at 1.7 V was observed. Therefore, the Li//SS half-cell was cathodically scanned to 1.7 V and held for 24 h to reach a quasi-steady-state (current is close to zero) (Figure S1b). Cathodic scanning to 1.7 V followed with potentiostatic process is denoted as PS1. A rapid current decrease occurred during the voltage holding due to the formation of passivated interphase by reduction of the electrolytes. To build a more robust surface passivation layer, the PS1 process was repeated for 5 times in the voltage of 1.7–4.6 V, referred as PS5. As a control, scanning with a voltage range in 2.8–4.6 V for 5 cycles without voltage holding was also performed, in which less electrolyte reduction occurred, and this process was referred as Base5. The anodic stability was evaluated using LSV. The pristine cell (Base) showed significant increase in anodic current above ≈4.2 V, indicative of oxidation of LiDFOB and FEC (Figure 1a).[43,59] And the current was slightly lowered in Base5, indicating that the oxidative products are barely passivated to the surface. In contrast, the pre-potentiostatic cells displayed significantly reduced oxidation currents and enhanced voltage stabilities, up to 5 V in PS5. Therefore, the formed layer should be able to protect the cathode at high voltage.

To explore the possibility of CEI formation on cathode by pre-potentiostatic discharge process in LiDFOB-$LiBF_4$ electrolyte, LCO//Li coin-type cells were tested using single-crystalline LCO cathodes with an areal capacity of 1.5 mAh cm^{-2}, excessive lithium anodes (550 μm) and 80 μL electrolyte. The reductive decomposition of the electrolyte on LCO surface mainly occurred at ≈1.7 V, similar with that of Li//SS cells, as revealed by galvanostatic discharge profile at a very small current rate of 2 mA g^{-1} and LSV curve (inset of Figure 1b). During the pre-potentiostatic discharge at 1.7 V, also denoted as PS1, a very small capacity of 8 mAh g^{-1} was delivered (Figure 1c), with a slight increase in Li content of LCO electrode, showing that the capacity was mainly contributed by the decomposition of electrolyte to form CEI.

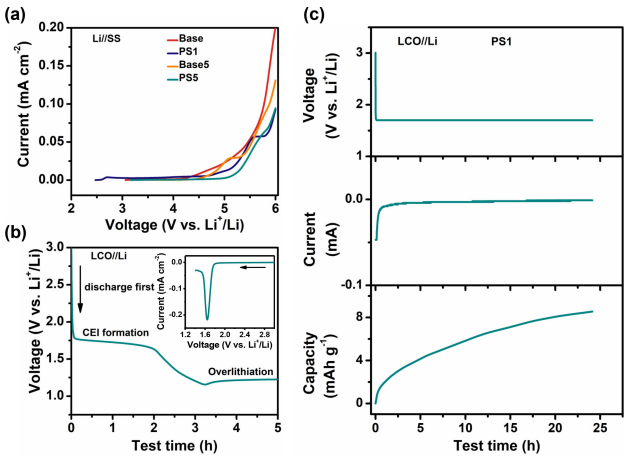

Figure 1. Oxidative and reductive behavior of LiDFOB-$LiBF_4$ electrolyte on stainless-steel (SS) and LCO with or without potentiostatic steps. a) LSV curves of LiDFOB-$LiBF_4$ electrolyte with or without pre-potentiostatic steps in Li//SS cells at a scanning rate of 1 mV s^{-1}. b) Voltage profile for the initial discharge of LCO//Li cell at a current rate of 2 mA g^{-1} and LSV curve (inset) at a sweep rate of 0.1 mV s^{-1}. c) Evolution of the current and capacity of LCO//Li cell in PS1.

The effects of pre-potentiostatic voltage on the CEI formation was investigated by applying voltages of 2.0, 1.4, 1.0 V and external electrical shorting (0 V) for 10 or 20 s on LCO//Li cells, referred as PS-2V, PS-1.4V, PS-1V and short-10s or short-20s, respectively. Figure S2 shows the current/capacity profiles during the discharge and potentiostatic process at different voltages over 24 h. In PS-2V, no obvious current and capacity responses were detected (Figure S2a), indicating minor electrolyte reduction. When the potentiostatic voltage was lowered to 1.4 V, electrolyte reduction occurred without obvious intercalation of Li in LCO (Figure S2b). However, during PS-1V, a huge current was measured with a capacity of 785 mAh g^{-1} (Figure S2c), much larger than those at higher voltages. Apparently, this came from the excessive intercalation of Li in LCO, which caused severe structural damage of LCO, as revealed by the scanning electron microscopy (SEM) images (Figure S3) and X-ray diffraction (XRD) patterns (Figure S4) of the pre-potentiostatic LCO cathodes. Although no detectable structural damage was observed for the 10 or 20 s electrical shorting, it is a non-controllable process to form CEI. Therefore, to avoid damaging LCO and constructing effective CEI, 1.7 V was applied for the potentionstatic process. The effectiveness of the 1.7 V potentionstatic process was verified by the cycling stability enhancement of LCO as well as the good morphology and sustained structural integrity after cycling (Figure S5–S7). However, cracking occurred on the cycled LCO particles in other procedures due to the lack of effective surface protection and volume change (Figure S6). The volume change comes from the accumulation of irreversible structure transitions from H1 to H2 and H3, which were observed as newly appeared peaks at lower degree than the (003) peak in XRD patterns (Figure S7),[60–62] and thereby causes the worse stabilities.

To form more robust CEI layers on LCO, PS5 process was performed. The potentiostatic capacities in five cycles were between 6–9 mAh g^{-1}, which is for self-repairing of CEI (Figure S8 and Figure 2a). To probe the anodic stability of the CEI layer on LCO, aggressive electrochemical test by charging the LCO cathode to 4.6 V versus Li^+/Li and holding for 180 h was carried out. A very small quasi-steady-state leakage current of 0.0014 mA cm^{-2} was measured for the LCO cathode with PS5 compared with those without

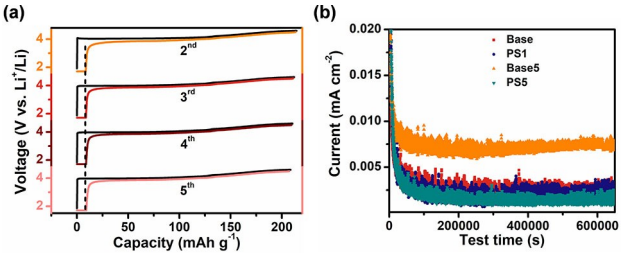

Figure 2. High-voltage stability of CEI formed on LCO via 1.7 V potentiostatic process. a) Voltage profiles of LCO//Li cell in PS5 under 0.5C. b) Leakage current comparison during 4.6 V constant-voltage floating test with or without voltage hold at 1.7 V.

potentiostatic discharge process (Base and Base5) (Figure 2b). The large current for the LCO cathode with Base5 (0.007 mA cm^{-2}) indicated that continuous side reactions occurred when cycling at a high voltage, while the side reactions were effectively retarded by the PS5 process.

To have insights into the CEI formation in the 1.7 V potentiostatic process, the PS5 and Base5 processed LCO cathodes were investigated by SEM and high-resolution transmission electron microscopy (HRTEM). The Base5 processed LCO showed a rough surface (Figure 3c, d) compared with a smooth surface for the pristine electrode (Figure 3a, b). This may be associated with the instable oxidative decomposition products of LiDFOB and FEC at a high voltage. In contrast, an obvious coating layer was observed after PS5 process (Figure 3e, f). It is worth noting that numerous ultra-small particles in diameters of 1–2 nm were displayed with a gradient distribution, higher density in the inner layer and less in the outer layer. The nanoparticles should be crystalline LiF phase (PDF no. 45-1460), as verified by embedded selected-area electron diffraction (SAED) pattern. The results are consistent with Lucht's observations of the nanostructured LiF derived from LiDFOB reduction on Li metal anodes.[50] As expected, a LiF-rich CEI was successfully induced by potentiostatic discharge process and would overcome some intrinsic traits of normal CEI layer, such as heterogeneous, adsorptive and dynamic,[20,54] thus shielding the bulk LCO against further electrolyte attack.

The chemical compositions of the CEI layers on LCO after PS5 and Base5 procedures were investigated using X-ray photoelectron spectroscopy (XPS). As displayed in Figure 3g, pronounced peaks at 685.1 and 56.5 eV in the F 1s and Li 1s spectra, assigned to flourishing LiF, appeared with PS5, while they were indetectable with Base5. This proves the formation of LiF-rich CEI via potentiostatic discharge process and the CEI layer was thicker than that formed in Base5, as suggested by the weaker peaks of Co–O (530.5 eV)[15] and C–C (284.8 eV). Apparently, the difference should be induced by the different reductive and oxidative decomposition behaviors of the electrolyte. Upon reduction in PS5, LiDFOB preferentially decomposed to form LiF and $Li_xBO_yF_z$ compounds as well as Li_2CO_3, lithium alkyl carbonates, and lithium oxalate species.[50–52] The reducibility of LiDFOB was further verified by the absence of reduction reaction at about 1.7 V in the electrolytes without LiDFOB (Figure S9). However, at high voltages, LiDFOB and FEC tend to be oxidized to organic-rich species, such as $(CO_2BF_2)_2$ dimers,[44,45] as evidenced by the characteristic peaks of B–O/C–O and C=O. The formation of LiF via potentiostatic reduction was also revealed by conspicuous LiF signals of F 1s and Li 1s in PS1 (Figure S10), but less than in PS5.

The depth distribution of CEI layers was investigated by Ar ion etching for ≈5 and 20 nm through 5 and 20 min Ar^+ sputtering. The LiF signal of the LCO cathode with PS5 became stronger after 5 nm sputtering compared with that no sputtering, suggesting a gradient distribution of the CEI layer, with more LiF in the inner and less in the outer (Figure S11a, S11b). Correspondingly, weak and barely

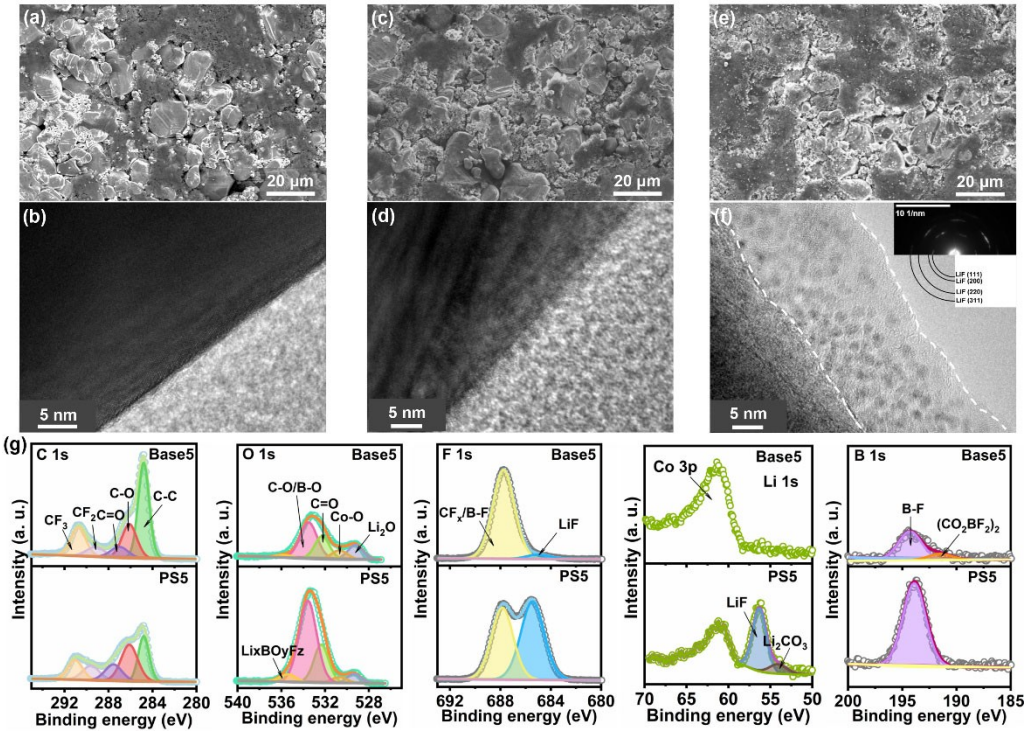

Figure 3. Structural and chemical characterization of CEI films. SEM and HRTEM images of a), b) pristine (fresh) LCO electrodes. CEI formed in c), d) Base5 and e), f) PS5. SAED pattern is shown in the inset. g) XPS spectra revealing the surface chemistry difference under two conditions.

changed Co signal were detected within 5 nm (Figure S11b), indicating that the ion etching didn't reach the LCO surface. However, LiF became less while Co signal enhanced after 20 nm sputtering, implying the CEI layer has been run through and Co signal was collected. It can be concluded that the thickness of the CEI layer formed with the PS5 process is between 5–20 nm. In contrast, much less amount of LiF was detected in the Base5 process, accompanied with continually increasing Co fraction during the sputtering, showing that a thin CEI layer with less LiF was formed (Figure S11c). These results agree well with the TEM observations and prove the ability of LiDFOB-$LiBF_4$ electrolyte to construct robust LiF-rich CEI layers via potentiostatic reduction.

The effects of the resulting CEI layers on the electrochemical performance of LCO cathode were investigated by using a high cut-off voltage of 4.6 V, at which a high capacity is achievable (Figure 4). Capacities of $\approx$200 mAh g^{-1} were obtained at 0.5C for LCO cathodes (Figure 4a). The Base LCO cathode suffered a rapid capacity decay with only 17.4 % capacity retention after 400 cycles and fluctuating Coulombic efficiencies (CEs) at an average of 99.24 %. In sharp contrast, significantly enhanced cycling stability was demonstrated for the PS-processed cathodes. The PS5 cathode achieved slightly better cycling performance than PS1 with a high capacity retention of 63.5 % and a high average CE of 99.58 %. Stable and high CE suggest limited side reactions between the LCO cathode and electrolyte at a high voltage. For comparison, a longer voltage holding time of 120 h, equivalent to the overall potentiostatic time used in

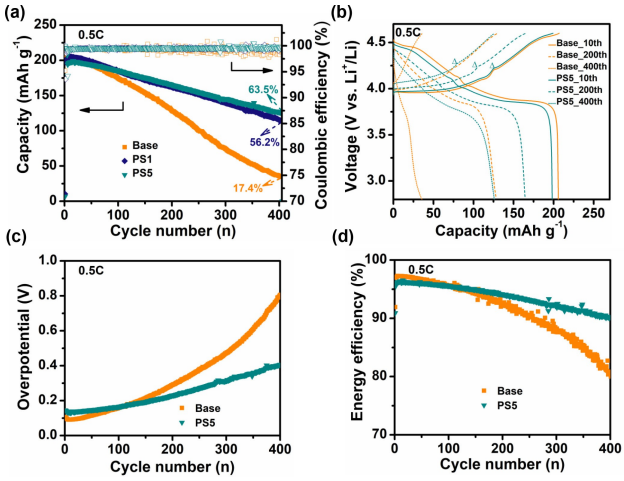

Figure 4. Electrochemical performance of LCO//Li cells with and without LiF-rich CEI. a) Long-term cycling stability, b) voltage profiles (the triangles in the profile indicate distinct phase transition), c) overpotentials ($\Delta U = U_{ch} - U_{disch}$, where U_{ch} and U_{disch} are the average charge and discharge potential vs Li^+/Li), and d) energy efficiency under 0.5C. Note that, the number of cycles in PS5 towards voltage profiles, overpotentials and energy efficiency was calculated after deducting five potentiostatic cycles. All cells were tested at a constant temperature of 25 °C within 2.8–4.6 V except for the potentiostatic steps.

PS5, was also applied, referred as PS-120h. Slightly worse cycling stability was displayed than PS5 (57.1 % vs 63.5 % capacity retentions) (Figure S12). Therefore, LiF-rich CEI

after self-healing process is better than one-time formed LiF-rich CEI. A much slower increase in overpotential was presented for the PS5 cathode than the Base cathode (Figure 4b, c). Therefore, an impressive energy efficiency of 90.2 % after 400 cycles was retained for PS5, versus 80.4 % for Base (Figure 4d). The former is sufficient for the application of next-generation high-voltage cathodes.[4] In addition, the rate capability of LCO could also be improved by potentiostatic process, especially for PS1 due to the better kinetics than that of PS5 (Figure S13a). Consequently, the PS1 cell at a higher rate of 1C delivered better cycling performance than Base cathode, as evidenced by the higher retention of capacity (77.8 %) and CE (averagely 99.8 %) over 400 cycles (Figure S13b). Likewise, the smaller overpotential and higher energy efficiency were observed than those of Base (Figure S13c, S13d). These results strongly highlight the effective protection of the designed CEI via potentiostatic reduction on LCO.

To understand the protection of LiF-rich CEI on the LCO cathode after long cycling (400 cycles), focused ion beam and SEM (FIB-SEM) and time-of-flight secondary ion mass spectrometry (TOF-SIMS) were used. The FIB-SEM cross-section images were presented in Figure 5a, b. As highlighted by the yellow rectangles, extensive cracks were observed in the bulk LCO particle of Base penetrating from surface to interior (Figure 5a). Contrarily, LCO cathode in PS5 maintained intact morphology without cracks (Figure 5b), highlighting that the irreversible structural transition by electrolyte penetration were effectively suppressed by the LiF-rich CEI layer, which could stably exist during cycling, as revealed by TOF-SIMS observation (Figure 5c–g and Figure S14). The acquisition was performed using Ga^+ ion beam in negative-ion modes covering the same field of view of 2×2 μm^2 with sputtered depth of around 230 nm. As indicated in the spatial elemental mapping and corresponding depth distributions of the LCO cathode, the fragment of F^- (mass/electron charge $(m/z)=19$) was detected on the upper surface with decreasing intensity, accompanied by an increasing O^- (mass/electron charge $(m/z)=16$), indicative of the lattice oxygen in the LCO cathode bulk phase (Figure 5e–g and Figure S14a). Thus, the LiF-rich CEI layer formed in the PS5 process behaves a high sustainability after cycling. In sharp contrast, little change of O^- and F^- as well as the very small fraction of F^- were detected with Base process, suggesting that there is no sustainable CEI layer formed on the LCO surface during cycling (Figure 5c, d, g and Figure S14b).

The LiF-rich CEI could effectively suppress interfacial side reactions between the highly oxidized cathode and the electrolyte, and thus prevent the Co species from leaching out from LCO. Lower Co contents with PS5 than Base in cycled electrolytes were detected by inductively coupled plasma mass spectrometry (ICP-MS) measurements (1.56 ppm vs 2.64 ppm at 5th and 6.08 ppm vs 13.1 ppm at 150th) (Figure 5h), confirming a less structural damage after PS5 process. Furthermore, the resistance after different

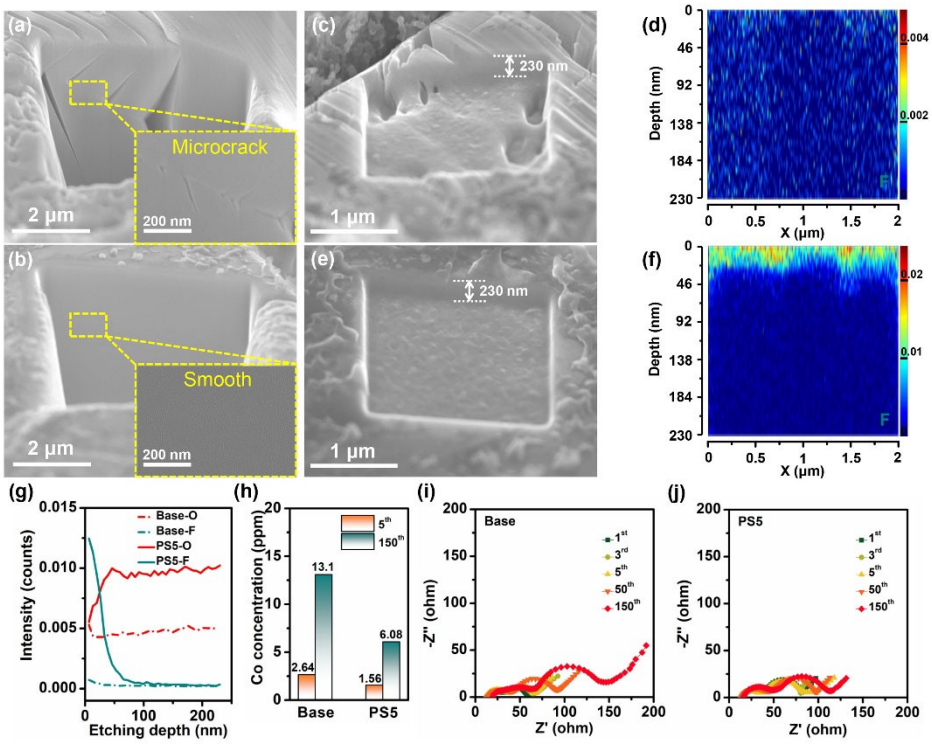

Figure 5. Morphological analysis and EIS characterization of LCO electrodes and LCO//Li cells after cycling. Cross-sectional SEM images of LCO extracted in a) Base and b) PS5. The crater sputtered by a Ga^+ ion beam and the spatial F mapping in c), d) Base and e), f) PS5. g) Depth profiles distribution of F and O. h) Comparison of transition metal Co ion contents in electrolytes extracted from the LCO//Li cells after different cycles in Base and PS5. Evolutions of Nyquist plots of LCO//Li cells with i) Base and j) PS5 at 4.6 V after 1, 3, 5, 50, and 150 cycles.

cycles was measured by electrochemical impedance spectroscopy (EIS) and collected at charged state (4.6 V) (Figure 5i,j). The Nyquist plots of the cells mainly consist of two depressed semicircles at high frequency, representing the interfacial resistance (R_f) and charge transfer resistance (R_{ct}), and a slop line at low frequency corresponding to lithium diffusion.[13] Observably, although larger R_f and R_{ct} in the initial cycles were displayed due to the formation of LiF-rich CEI layer in PS5, a relatively stable resistance with cycling was observed and lower than that of Base after 150 cycles. Once again, the designed LiF-rich CEI offers significant advantages in stabilizing LCO cathode at a high cut-off voltage of 4.6 V.

To evaluate the potential of practical application, LCO//graphite full cells with a practical areal capacity of 3 mAh cm^{-2} were fabricated and tested in a voltage range of 2.80–4.55 V (equivalent to 4.6 V versus Li^+/Li). As represented by Figure S15a, the LCO cathode exhibited the best cycling performance in PS1 with a capacity of 2.82 mAh cm^{-2} at 0.5C due to the kinetic limit of high-loading electrodes. The graphite anodes delivered a capacity of 2.90 mAh cm^{-2} under the same current (Figure S15b), which would yield an N/P ratio of 1.03/1 in the full-cell configuration. Thus, the PS1 processed LCO electrodes were extracted and reassembled with fresh graphite anodes. Figure 6a shows the potential vs. specific capacity plots of full cells at 0.5C. A high capacity of 100 mAh g^{-1} based on total mass of LCO cathode and graphite anode was delivered in the 10th cycle with a high operating voltage of 3.80 V, corresponding to a high energy density of 380.70 Wh kg^{-1}. The initial Coulombic efficiency reached 85.0 %, which is almost the same as the

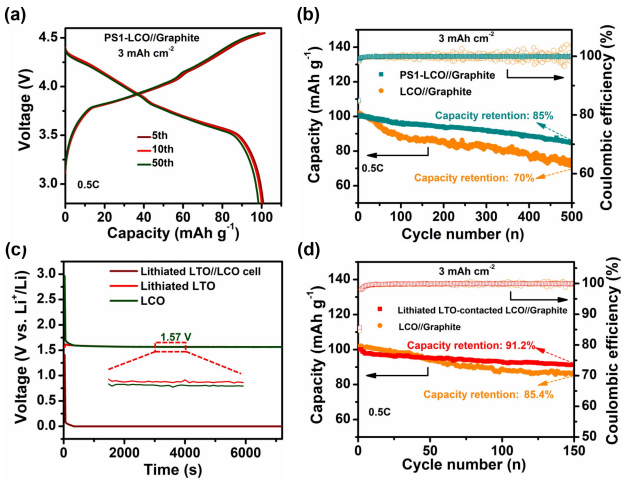

Figure 6. Electrochemical performance of LCO//Graphite full cells. a) Galvanostatic voltage profiles of LiF-rich CEI protected LCO//Graphite coin cell and b) comparison of long-term cycling stability of full cells at 0.5C (25 °C, 2.80–4.55 V). Demonstration of lithiated LTO electrodes for the LiF-rich CEI construction in full cell. c) Potential monitored by a three-electrode coin cell using a small piece of lithium metal as a reference electrode between lithiated LTO and LCO and d) enhanced cycling performance with lithiated LTO-contacted LCO//graphite full cell (held the lithiated LTO//LCO cell at 0 V) (25 °C, 0.5C, 2.80–4.55 V). Note, all the capacities are calculated based on the total mass of LCO cathode and graphite anode.

LCO//Graphite full cell without the PS1 process (84.6 %). More importantly, significant enhancement in cycling stability was realized with the PS1 process, with a higher capacity retention of 85 % and more stable CE, averagely 99.9 % over 500 cycles than those of LCO//graphite cells without the PS1 process (Figure 6b). The performance of high-voltage LCO is highly competitive in comparison with those reported in literature (Table S1). The enhanced cyclability of the PS1 processed LCO//graphite full cell was mainly attributed to the effective protection of LiF-rich CEI on LCO cathode, as revealed by SEM image of the cycled LCO which shows few cracks (Figure S16b). Consequently, the cycled graphite electrodes presented more uniform and smaller deposits of F, O and B-containing species than that of Base (Figure S17, S18).

The PS pretreatment of LCO cathodes can be replaced by simply connecting LCO to lithiated lithium titanium oxide (LTO) anodes in present of electrolytes since LTO has a flat reaction platform at 1.5 V (Figure S19). The lithiated LTO can act as a stable lithium source offering Li^+ to do the PS process. To monitor the LCO potential during shorting the LCO and lithiated LTO, a three-electrode coin cell using a lithiated LTO anode, a LCO cathode and lithium as a reference electrode was configured. As shown in Figure 6c, when applying a current to decrease the cell voltage to 0 V, equal with physical contacting process between LCO and lithiated LTO, the potential of LCO vs Li^+/Li was precisely controlled at 1.57 V. Despite a lower voltage than that of 1.70 V in LCO//Li cell, the cyclability of the lithiated LTO-contacted LCO//graphite was improved with a higher capacity retention than the LCO//graphite cell without the PS1 process (91.2 % vs 85.4 %) (Figure 6d), proving the effectiveness of the formed CEI layer. Encouragingly, considering the more comprehensive and mature pre-lithiated technology and simple short-circuit operation process, formation of LiF-rich CEI on LCO cathode has been extended to NMC cathode, providing universal strategy to enhance the energy density of current NMC//graphite batteries.

Conclusion

LiF-rich CEI was formed on LCO cathode by potentiostatic reduction of 1.0 M LiDFOB–0.2 M $LiBF_4$-FEC-DEC electrolyte at 1.7 V without decomposing the cathode. The robust LiF-rich CEI significantly enhanced the cycling stability of 4.6 V high-voltage LCO as a result of suppressed structural damage, electrolyte penetration and Co dissolution. A long-life LCO//graphite full cell using LCO with LiF-rich CEI has been demonstrated with a capacity retention of 85 % over 500 cycles at a practical areal capacity of 3 mAh cm^{-2}, maintaining an energy density of 313.3 Wh kg^{-1} (based on total mass of LCO cathode and graphite anode). Forming LiF-rich CEI on high voltage cathodes by electrolyte reduction provides promising insight into designing effective electrolyte formulations for next generation of high energy and long cycle life Li-ion batteries.

Acknowledgements

This work was supported by Tianjin University International Education Program For Outstanding Doctoral Thesis.

Conflict of Interest

The authors declare no conflict of interest.

Data Availability Statement

The data that support the findings of this study are available from the corresponding author upon reasonable request.

Keywords: Fluorinated Electrolyte · High-voltage Cathodes · LiF-rich Cathode-Electrolyte Interphase · Potentiostatic Reduction

[1] Z. Lin, T. Liu, X. Ai, C. Liang, *Nat. Commun.* **2018**, *9*, 5262.
[2] Q. Yang, J. Huang, Y. Li, Y. Wang, J. Qiu, J. Zhang, H. Yu, X. Yu, H. Li, L. Chen, *J. Power Sources* **2018**, *388*, 65–70.
[3] S. Ahmed, S. E. Trask, D. W. Dees, P. A. Nelson, W. Lu, A. R. Dunlop, B. J. Polzin, A. N. Jansen, *J. Power Sources* **2018**, *403*, 56–65.
[4] W. Xue, M. Huang, Y. Li, Y. G. Zhu, R. Gao, X. Xiao, W. Zhang, S. Li, G. Xu, Y. Yu, P. Li, J. Lopez, D. Yu, Y. Dong, W. Fan, Z. Shi, R. Xiong, C.-J. Sun, I. Hwang, W.-K. Lee, Y. Shao-Horn, J. A. Johnson, J. Li, *Nat. Energy* **2021**, *6*, 495–505.
[5] R. Jung, M. Metzger, F. Maglia, C. Stinner, H. A. Gasteiger, *J. Phys. Chem. Lett.* **2017**, *8*, 4820–4825.
[6] S. S. Zhang, *Energy Storage Mater.* **2020**, *24*, 247–254.
[7] J. Qian, L. Liu, J. Yang, S. Li, X. Wang, H. L. Zhuang, Y. Lu, *Nat. Commun.* **2018**, *9*, 4918.
[8] Q. Liu, X. Su, D. Lei, Y. Qin, J. Wen, F. Guo, Y. A. Wu, Y. Rong, R. Kou, X. Xiao, F. Aguesse, J. Bareño, Y. Ren, W. Lu, Y. Li, *Nat. Energy* **2018**, *3*, 936–943.
[9] J.-N. Zhang, Q. Li, C. Ouyang, X. Yu, M. Ge, X. Huang, E. Hu, C. Ma, S. Li, R. Xiao, W. Yang, Y. Chu, Y. Liu, H. Yu, X.-Q. Yang, X. Huang, L. Chen, H. Li, *Nat. Energy* **2019**, *4*, 594–603.
[10] J. Li, C. Lin, M. Weng, Y. Qiu, P. Chen, K. Yang, W. Huang, Y. Hong, J. Li, M. Zhang, C. Dong, W. Zhao, Z. Xu, X. Wang, K. Xu, J. Sun, F. Pan, *Nat. Nanotechnol.* **2021**, *16*, 599–605.
[11] X. Ding, D. Luo, J. Cui, H. Xie, Q. Ren, Z. Lin, *Angew. Chem. Int. Ed.* **2020**, *59*, 7778–7782; *Angew. Chem.* **2020**, *132*, 7852–7856.
[12] Y. Bi, J. Tao, Y. Wu, L. Li, Y. Xu, E. Hu, B. Wu, J. Hu, C. Wang, J. G. Zhang, Y. Qi, J. Xiao, *Science* **2020**, *370*, 1313–1317.
[13] X. Yang, M. Lin, G. Zheng, J. Wu, X. Wang, F. Ren, W. Zhang, Y. Liao, W. Zhao, Z. Zhang, N. Xu, W. Yang, Y. Yang, *Adv. Funct. Mater.* **2020**, *30*, 2004664.
[14] W. Xue, R. Gao, Z. Shi, X. Xiao, W. Zhang, Y. Zhang, Y. G. Zhu, I. Waluyo, Y. Li, M. R. Hill, Z. Zhu, S. Li, O. Kuznetsov, Y. Zhang, W.-K. Lee, A. Hunt, A. Harutyunyan, Y. Shao-Horn, J. A. Johnson, J. Li, *Energy Environ. Sci.* **2021**, *14*, 6030–6040.
[15] J. Zhang, P. F. Wang, P. Bai, H. Wan, S. Liu, S. Hou, X. Pu, J. Xia, W. Zhang, Z. Wang, B. Nan, X. Zhang, J. Xu, C. Wang, *Adv. Mater.* **2022**, *34*, 2108353.
[16] J. Mi, J. Ma, L. Chen, C. Lai, K. Yang, J. Biao, H. Xia, X. Song, W. Lv, G. Zhong, Y.-B. He, *Energy Storage Mater.* **2022**, *48*, 375–383.
[17] K. Xu, *Chem. Rev.* **2014**, *114*, 11503–11618.
[18] L. Yang, B. Ravdel, B. L. Lucht, *Electrochem. Solid-State Lett.* **2010**, *13*, A95–A97.
[19] D. Bedrov, O. Borodin, J. B. Hooper, *J. Phys. Chem. C* **2017**, *121*, 16098–16109.
[20] J.-N. Zhang, Q. Li, Y. Wang, J. Zheng, X. Yu, H. Li, *Energy Storage Mater.* **2018**, *14*, 1–7.
[21] X. Fan, C. Wang, *Chem. Soc. Rev.* **2021**, *50*, 10486–10566.
[22] X. Fan, X. Ji, F. Han, J. Yue, J. Chen, L. Chen, T. Deng, J. Jiang, C. Wang, *Sci. Adv.* **2018**, *4*, eaau9245.
[23] J. Chen, X. Fan, Q. Li, H. Yang, M. R. Khoshi, Y. Xu, S. Hwang, L. Chen, X. Ji, C. Yang, H. He, C. Wang, E. Garfunkel, D. Su, O. Borodin, C. Wang, *Nat. Energy* **2020**, *5*, 386–397.
[24] Y. Zhu, X. He, Y. Mo, *ACS Appl. Mater. Interfaces* **2015**, *7*, 23685–23693.
[25] N. von Aspern, G. V. Roschenthaler, M. Winter, I. Cekic-Laskovic, *Angew. Chem. Int. Ed.* **2019**, *58*, 15978–16000; *Angew. Chem.* **2019**, *131*, 16124–16147.
[26] T. Li, X.-Q. Zhang, P. Shi, Q. Zhang, *Joule* **2019**, *3*, 2647–2661.
[27] G. Cherkashinin, K. Nikolowski, H. Ehrenberg, S. Jacke, L. Dimesso, W. Jaegermann, *Phys. Chem. Chem. Phys.* **2012**, *14*, 12321–12331.
[28] X. Fan, L. Chen, O. Borodin, X. Ji, J. Chen, S. Hou, T. Deng, J. Zheng, C. Yang, S.C. Liou, K. Amine, K. Xu, C. Wang, *Nat. Nanotechnol.* **2018**, *13*, 715–722.
[29] X. Fan, X. Ji, L. Chen, J. Chen, T. Deng, F. Han, J. Yue, N. Piao, R. Wang, X. Zhou, X. Xiao, L. Chen, C. Wang, *Nat. Energy* **2019**, *4*, 882–890.
[30] Z. Yu, H. Wang, X. Kong, W. Huang, Y. Tsao, D. G. Mackanic, K. Wang, X. Wang, W. Huang, S. Choudhury, Y. Zheng, C. V. Amanchukwu, S. T. Hung, Y. Ma, E. G. Lomeli, J. Qin, Y. Cui, Z. Bao, *Nat. Energy* **2020**, *5*, 526–533.
[31] Z. Yu, P. E. Rudnicki, Z. Zhang, Z. Huang, H. Celik, S. T. Oyakhire, Y. Chen, X. Kong, S.C. Kim, X. Xiao, H. Wang, Y. Zheng, G. A. Kamat, M. S. Kim, S. F. Bent, J. Qin, Y. Cui, Z. Bao, *Nat. Energy* **2022**, *7*, 94–106.
[32] Q. Zheng, Y. Yamada, R. Shang, S. Ko, Y.-Y. Lee, K. Kim, E. Nakamura, A. Yamada, *Nat. Energy* **2020**, *5*, 291–298.
[33] J. Wang, Y. Yamada, K. Sodeyama, C. H. Chiang, Y. Tateyama, A. Yamada, *Nat. Commun.* **2016**, *7*, 12032.
[34] S. Jiao, X. Ren, R. Cao, M. H. Engelhard, Y. Liu, D. Hu, D. Mei, J. Zheng, W. Zhao, Q. Li, N. Liu, B. D. Adams, C. Ma, J. Liu, J.-G. Zhang, W. Xu, *Nat. Energy* **2018**, *3*, 739–746.
[35] X. Cao, X. Ren, L. Zou, M. H. Engelhard, W. Huang, H. Wang, B. E. Matthews, H. Lee, C. Niu, B. W. Arey, Y. Cui, C. Wang, J. Xiao, J. Liu, W. Xu, J.-G. Zhang, *Nat. Energy* **2019**, *4*, 796–805.
[36] X. Ren, X. Zhang, Z. Shadike, L. Zou, H. Jia, X. Cao, M. H. Engelhard, B. E. Matthews, C. Wang, B. W. Arey, X. Q. Yang, J. Liu, J. G. Zhang, W. Xu, *Adv. Mater.* **2020**, *32*, 2004898.
[37] W. Liu, J. Li, W. Li, H. Xu, C. Zhang, X. Qiu, *Nat. Commun.* **2020**, *11*, 3629.
[38] F. Wu, S. Fang, M. Kuenzel, A. Mullaliu, J.-K. Kim, X. Gao, T. Diemant, G.-T. Kim, S. Passerini, *Joule* **2021**, *5*, 2177–2194.
[39] J. Alvarado, M. A. Schroeder, T. P. Pollard, X. Wang, J. Z. Lee, M. Zhang, T. Wynn, M. Ding, O. Borodin, Y. S. Meng, K. Xu, *Energy Environ. Sci.* **2019**, *12*, 780–794.
[40] K. Xu, *Chem. Rev.* **2004**, *104*, 4303–4418.
[41] Z. Wang, Y. Sun, L. Chen, X. Huang, *J. Electrochem. Soc.* **2004**, *151*, A914–A921.
[42] M. Mao, B. Huang, Q. Li, C. Wang, Y.-B. He, F. Kang, *Nano Energy* **2020**, *78*, 105282.
[43] S. S. Zhang, *Electrochem. Commun.* **2006**, *8*, 1423–1428.

[44] I. A. Shkrob, Y. Zhu, T. W. Marin, D. P. Abraham, *J. Phys. Chem. C* **2013**, *117*, 23750–23756.
[45] J. Ma, Z. Liu, B. Chen, L. Wang, L. Yue, H. Liu, J. Zhang, Z. Liu, G. Cui, *J. Electrochem. Soc.* **2017**, *164*, A3454–A3461.
[46] Y. Qiao, H. Yang, Z. Chang, H. Deng, X. Li, H. Zhou, *Nat. Energy* **2021**, *6*, 653–662.
[47] L. Yu, Y. Tian, X. Xiao, C. Hou, Y. Xing, Y. Si, H. Lu, Y. Zhao, *J. Electrochem. Soc.* **2021**, *168*, 050516.
[48] S.-H. Kang, S.-H. Park, C. S. Johnson, K. Amine, *J. Electrochem. Soc.* **2007**, *154*, A268–A274.
[49] R. Robert, P. Novák, *Chem. Mater.* **2018**, *30*, 1907–1911.
[50] S. Jurng, Z. L. Brown, J. Kim, B. L. Lucht, *Energy Environ. Sci.* **2018**, *11*, 2600–2608.
[51] B. S. Parimalam, B. L. Lucht, *J. Electrochem. Soc.* **2018**, *165*, A251–A255.
[52] A. Xiao, L. Yang, B. L. Lucht, S.-H. Kang, D. P. Abraham, *J. Electrochem. Soc.* **2009**, *156*, A318–A327.
[53] W. Gu, O. Borodin, B. Zdyrko, H.-T. Lin, H. Kim, N. Nitta, J. Huang, A. Magasinski, Z. Milicev, G. Berdichevsky, G. Yushin, *Adv. Funct. Mater.* **2016**, *26*, 1507–1516.
[54] Z. Zhang, J. Yang, W. Huang, H. Wang, W. Zhou, Y. Li, Y. Li, J. Xu, W. Huang, W. Chiu, Y. Cui, *Matter* **2021**, *4*, 302–312.
[55] A. J. Louli, A. Eldesoky, R. Weber, M. Genovese, M. Coon, J. deGooyer, Z. Deng, R. T. White, J. Lee, T. Rodgers, R. Petibon, S. Hy, S. J. H. Cheng, J. R. Dahn, *Nat. Energy* **2020**, *5*, 693–702.
[56] E. R. Logan, A. J. Louli, M. Genovese, S. Trussler, J. R. Dahn, *J. Electrochem. Soc.* **2021**, *168*, 060527.
[57] L. Wang, B. Chen, J. Ma, G. Cui, L. Chen, *Chem. Soc. Rev.* **2018**, *47*, 6505–6602.
[58] Y. Lyu, X. Wu, K. Wang, Z. Feng, T. Cheng, Y. Liu, M. Wang, R. Chen, L. Xu, J. Zhou, Y. Lu, B. Guo, *Adv. Energy Mater.* **2021**, *11*, 2000982.
[59] C. Fu, Y. Ma, S. Lou, C. Cui, L. Xiang, W. Zhao, P. Zuo, J. Wang, Y. Gao, G. Yin, *J. Mater. Chem. A* **2020**, *8*, 2066–2073.
[60] L. Wang, J. Ma, C. Wang, X. Yu, R. Liu, F. Jiang, X. Sun, A. Du, X. Zhou, G. Cui, *Adv. Sci.* **2019**, *6*, 1900355.
[61] Y. Huang, Y. Zhu, H. Fu, M. Ou, C. Hu, S. Yu, Z. Hu, C. T. Chen, G. Jiang, H. Gu, H. Lin, W. Luo, Y. Huang, *Angew. Chem. Int. Ed.* **2021**, *60*, 4682–4688; *Angew. Chem.* **2021**, *133*, 4732–4738.
[62] J. Wan, J. Zhu, Y. Xiang, G. Zhong, X. Liu, Y. Li, K. H. L. Zhang, C. Hong, J. Zheng, K. Wang, Y. Yang, *J. Energy Chem.* **2021**, *54*, 786–794.

Manuscript received: February 19, 2022
Accepted manuscript online: April 8, 2022
Version of record online: April 28, 2022